ISSN 0915-633X

NATIONAL INSTITUTE FOR FUSION SCIENCE

Electromagnetic Instability and Anomalous Resistivity in a Magnetic Neutral Sheet

M. Ozaki, T. Sato, R. Horiuchi
and the Complexity Simulation Group

(Received - Dec. 20, 1995)

NIFS-393 Dec. 1995

RESEARCH REPORT
NIFS Series

NAGOYA, JAPAN

Electromagnetic Instability and Anomalous Resistivity in a Magnetic Neutral Sheet

Masao **OZAKI**[a], Tetsuya **SATO**, Ritoku **HORIUCHI**,
and the Complexity Simulation Group[b]

Theory and Computer Simulation Center, National Institute for Fusion Science, Nagoya 464-01, Japan

An electromagnetic instability in a magnetic neutral sheet is investigated by means of a $2\frac{1}{2}$ semi-implicit particle simulation code. Electromagnetic waves are excited slowly in a field null region after saturation of the lower hybrid drift waves excited in an early time on both sides of the neutral sheet. This instability is found to be a new instability, independent of the lower hybrid drift instability. Examination of its characteristic properties indicates that the new instability is highly related to the meandering motions of ions in the neutral sheet. The growth of the instability gives rise to anomalous resistivity in the neutral sheet current.

[a]On leave from *the Institite of Industrial Science, University of Tokyo.*

[b]K. Watanabe, T. Hayashi, Y. Todo, T. H. Watanabe, A. Kageyama, and H. Takamaru.

KEYWORDS: new electromagnetic instability, neutral sheet, ion meandering motion, anomalous resistivity, lower-hybrid instability

1. INTRODUCTION

Magnetic reconnection[1] is thought to be one of the most attractive and important concepts in space and laboratory plasmas, because it plays a vital role in an explosive energy release process such as solar flares and magnetospheric substorms, and in plasma confinement, such as tokamak sawteeth and disruptions.

The primary role of magnetic reconnection is to change the topology of magnetic field lines and to convert a stored magnetic energy swiftly to plasma kinetic energy. It is well known that electrical resistivity plays a crucial role in triggering magnetic reconnection. However, violent phenomena triggered by magnetic reconnection are often observed in a rarefied and high temperature plasma, in which binary collisions between particles hardly occur, namely, in a collisionless plasma. In this respect, Horiuchi and Sato[2] has recently demonstrated that magnetic reconnection can be driven in a collisionless plasma without invoking a direct generation of wave-induced anomalous resistivity. However, anomalous resistivity caused by unstable waves still remains to be a possible cause of collisionless reconnection.

Many kinds of instability have been proposed so far as candidates of anomalous resistivity in a neutral sheet region. Ion acoustic instability was proposed to explain anomalous resistivity in laboratory plasmas[3,4], but it required such a high ratio of electron temperature to ion temperature as $T_e/T_i \gtrsim 10$. Thus, ion acoustic instability is unlikely to occur in a normal condition. Because the diamagnetic drift speed in the neutral sheet is usually much lower than the electron thermal speed, Buneman instability is neither expected to occur.

Among these instabilities, the lower hybrid drift instability (LHDI)[5-12], which has a large growth rate and saturation amplitude, has attracted the attension of fusion plasma experimentists and space plasma physicists. Krall and Liewer[5] proposed that the LHDI could be excited in the vicinity of the neutral sheet and showed that the low frequency wave ($\Omega_{ci} < \omega < \Omega_{ce}$; Ω_{ci}, Ω_{ei} are ion and electron cyclotron frequencies, respectively) becomes unstable for any ratio of T_e/T_i. But the local and nonlocal studies show[7,12] that the growth rate of this instability does depend on the plasma beta (ratio of plasma pressure to magnetic pressure) and becomes vanishingly small in a high beta region. In other words, the LHDI must be localized somewhat away from the neutral sheet and the eigenfunction does not reach to the field null region.

Generally, it is difficult to solve self-consistently the nonlinear process in an imhomogeneous region (neutral sheet), by means of the mathematical methodology alone. The previous numerical simulations[10-12] have shown that sufficiently large growth of the LHD wave is observed away from the neutral sheet, but the unstable region cannot penetrate into the field null region. This implies that the LHDI cannot be directly responsible for anomalous resistivity in the neutral sheet. On the other hand, some simulations[9,11,12] have shown that a growing mode is excited at the center of the neutral sheet. Nevertheless, little attention has been given to this mode, nor its physical characteristics and roles have been studied in a satisfactory way. The true nature of the mode and associated anomalous resistivity remain to be revealed.

In section 2 we describe the fundametal equations, the initial condition, the

boundary condition used for the present simulation study. Simulation results are described in section 3 in the following order: First, the development of an electromagnetic instability in the neutral sheet is demonstrated. Then, independence of this electromagnetic instability from the lower hybrid instability is discussed and the amount of generated anomalous resistivity is derived. Also, the parameter dependence is investigated to examine the nature of the electromagnetic instability in the neutral sheet. Summary is given in section 4.

2. SIMULATION MODEL

We use a $2\frac{1}{2}$ semi-implicit particle simulation code[2,12,13], in which the time-decentered discretization technique is used for time advancing and the implicit algorithm is used for the field equations. By using this technique and taking a large time step, high frequency modes are eliminated, so that the desired low frequency phenomena can be resonably well dealt with.

The equations to be solved are Maxwell's equations,

$$\mathrm{rot}\boldsymbol{E} = -\frac{1}{c}\frac{\partial \boldsymbol{B}}{\partial t}, \tag{1}$$

$$\mathrm{rot}\boldsymbol{B} = \frac{4\pi}{c}\boldsymbol{j} + \frac{1}{c}\frac{\partial \boldsymbol{E}}{\partial t}, \tag{2}$$

$$\mathrm{div}\boldsymbol{E} = 4\pi\rho, \tag{3}$$

$$\mathrm{div}\boldsymbol{B} = 0, \tag{4}$$

and the equations of motion

$$\frac{d}{dt}(\gamma_j \boldsymbol{v}_j) = \frac{q_j}{m_j}(\boldsymbol{E} + \frac{\boldsymbol{v}_j}{c} \times \boldsymbol{B}), \tag{5}$$

$$\frac{d\boldsymbol{x}_j}{dt} = \boldsymbol{v}_j, \tag{6}$$

where $\boldsymbol{x}_j(t)$, $\boldsymbol{v}_j(t)$, m_j, and q_j are the position, the velocity, the rest mass, and the charge of the jth particle, and the relativistic γ factor of the jth particle is defined by

$$\gamma_j = 1/\sqrt{1-(\boldsymbol{v}_j \cdot \boldsymbol{v}_j)/c^2} \tag{7}$$

The current density $\boldsymbol{j}(\boldsymbol{x},t)$ and the chrage density $\rho(\boldsymbol{x},t)$ are defined by summing up all the particles,

$$\boldsymbol{j}(\boldsymbol{x},t) = \sum_{j=1}^{N} q_j \boldsymbol{v}_j(t) S[\boldsymbol{x} - \boldsymbol{x}_j(t)], \tag{8}$$

$$\rho(\boldsymbol{x},t) = \sum_{j=1}^{N} q_j S[\boldsymbol{x} - \boldsymbol{x}_j(t)], \tag{9}$$

where N is the total number of particles, and $S(\boldsymbol{x})$ is the form function of particles, which is expressed by a triangle with the base length equal to twice the grid separation.

We numerically solve the time evolution of these field-particle coupled equations, eqs. (1), (2), (5), (6) and (8). Equations (3) and (4) are initially satisfied. Spatial homogeneity in z-direction ($\partial/\partial z = 0$) is assumed, namely, a two-dimensional geometry is chosen.

As an initial condition, we adopt the MHD equilibrium

$$\frac{1}{c}\boldsymbol{j} \times \boldsymbol{B} = \nabla p \tag{10}$$

with the Harris-type antiparallel magnetic field configuration[12], namely,

$$B_z(y) = B_0 \tanh(y/L), \tag{11}$$

$$j_x(y) = j_0 \, \mathrm{sech}^2(y/L), \tag{12}$$

$$p(y) = p_0 \, \mathrm{sech}^2(y/L), \tag{13}$$

where $j_0 = cB_0/4\pi L$, $p_0 = B_0^2/8\pi$, and L is the scale height along the y axis. There is a magnetic neutral sheet along the mid-horizontal line ($y = 0$) in the initial equilibrium. We assume the electric field initially to be zero in the entire simulation box. We also assume that the initial particle distribution is a shifted-Maxwellian with a spatially constant temperature, and the average particle velocity is equal to the diamagnetic drift velocity. The drift speed of electrons and ions V_{de}, V_{di}, and the temperatures T_e, T_i, satisfy the relation, $V_{de}/T_e = -V_{di}/T_i$, which means the charge neutrality condition. The particle position and velocity are determined from the pressure and the current density. For the sake of numerical stability, one third of the whole particles are loaded as the background particles which have no diamagnetic drift velocity. Both an ion and an electron are loaded at the same position at the initial time.

In the actual calculations all variables are normalized by the following four basic quantities: c (velocity of light), e (elementary charge), m_e (electron mass), ω_{pe0} (electron plasma frequency defined as $\omega_{pe0} = \sqrt{4\pi n_0 e^2/m_e}$, where n_0 is the average total number density in the system). Accordingly, the time, the length, the electric field, and the magnetic field are normalized by ω_{pe0}^{-1}, c/ω_{pe0}, $m_e c\omega_{pe0}/e$, $m_e c\omega_{pe0}/e$, respectively.

The simulation region is a rectangular box which is bounded by $x = 0$, $x = L_x$, $y = -L_y$, and $y = L_y$. The periodic condition is imposed at the boundaries, $x = 0$ and $x = L_x$. The simulation domain ($L_x \times L_y$) is divided into 67×67 grids. The

number of loaded particles is 120000; hence the average particle number density is about 27 particles per cell.

3. SIMULATION RESULTS

Typical simulation parameters are as follows: the mass ratio is $m_i/m_e = 180$, the magnetic field intensity is $B_0 = 0.3\ m_e c\omega_{pe0}/e$, the scale height of the initial magnetic field is $L = 5\ c/\omega_{pe0}$, the simulation region is $L_x = 30\ c/\omega_{pe0}$ and $L_y = 32\ c/\omega_{pe0}$. The Alfvén transit time τ_A ($= L/V_A$, where $V_A = B_0/\sqrt{4\pi n_0 m_i}$ is the Alfvén velocity) becomes about 223 ω_{pe0}^{-1} for these parameters. The temperature ratio is $T_i/T_e = 2$ and the ratio of the ion drift velocity to the ion thermal velocity is $V_{di}/V_{thi} \simeq 2.1$.

A. Development of two independent electromagnetic instabilities

Figure 1 shows the time development of the magnetic field in $x - y$ plane. The left panels are the contours of $z-$component of the total magnetic field B_z and the right panels the contours of $z-$component of the perturbed magnetic field δB_z. (The maximum and minimum values are indicated on the top part of the panels.) The distribution of B_z (δB_z) along the y axis at $y = 0$ is shown in the upper margin and the distribution along the x axis at $x = 15\ c/\omega_{pe0}$ is shown in the right margin. At $T = 800\ \omega_{pe0}^{-1}$ a wavy structure in the contour lines is observed on both sides of the field null region, but one cannot see any appreciable penetration of the side modes into the field null region. Because of the particle diffusion caused by the modes, the density profile becomes less steep and the modes stop growing. At $T = 2800\ \omega_{pe0}^{-1}$ a new large scale wavy structure

appears at the field null region. At $T = 4000\ \omega_{pe0}^{-1}$ this new wavy structure at the field null region becomes remarkable and the amplitude reaches more than a half of the initial magnetic field. Thereafter it is gradually decaying, but at $T = 8000\ \omega_{pe0}^{-1}$ the structure still remains significantly.

Figure 2 shows the time development of the electric field. The left and right panels are the contours of x and y component of the electric field, respectively. As can be seen clearly at $T = 800\ \omega_{pe0}^{-1}$, fluctuations appear on the both sides of the field null region. But the value at the field null region remains small. After $T = 2800\ \omega_{pe0}^{-1}$ there appear electric field fluctuations around $y = 0$. However, the structure is more like the side modes and no clear one-to-one correspondence to the magnetic modes of Fig. 1.

Figure 3 shows arrow plot of the electron flow vector. (The maximum speed is indicated on the top shoulder of each panel.) On carefully examining the arrow plot one can find a small vortex structure corresponding to the side modes. However, the structure is not so conspicuous as the central modes. The central modes appear in the plot at $T = 2800\ \omega_{pe0}^{-1}$. The snaky structure develops more at $T = 4000\ \omega_{pe0}^{-1}$. Thereafter the structure gradually decays as is seen at $T = 8000\ \omega_{pe0}^{-1}$. We note that the ion flow is not shown here because the structure cannot be seen so clearly as the electron flow.

B. Lower hybrid drift instability

Let us now attempt to identify the observed two modes, *i.e.*, side modes and central modes. Figure 4 shows the dispersion relation at $y = 0$ and at $y = 5\ c/\omega_{pe0}$. The circles in Fig. 4(a) show the dispersion relation of E_x at

$y = 5\ c/\omega_{pe0}$, which is obtained by the Fourier spectrum, and the solid lines show the analytical dispersion relation of the LHDI[7], namely,

$$\omega = kV_{di}\frac{2\omega_{pi}^2}{k^2 v_{thi}^2}\left(1 + \frac{2\omega_{pi}^2}{k^2 v_{thi}^2} + \frac{\omega_{pe}^2}{\Omega_{ce}^2}\right)^{-1} \tag{14}$$

where Ω_{ce} is the electron cyclotron frequency and ω_{pi} is the ion plasma frequency. A fairly good agreement is seen between the numerical and analytical results with respect to the modes less than sixth. The open square in Fig. 4(b) show the dispersion relation of B_z at the field null region. Obviously, the dispersion relationship is quite different from that of the LHDI and the frequencies are on the order of the ion cyclotron freqency.

We shall next examine the spacio-temporal evolution of the Fourier-expanded mode in the x direction. Shown in Fig. 5 is the evolution pattern of the lowest six Fourier modes of the magnetic field B_z in $y - t$ domain. In the early phase, $\mathrm{m}_x = 5$ and 6 modes grow in the regions with steep density gradient, though not so clearly seen because of the low amplitude. In contrast, m_x =1 and 2 modes grow gradually at the center of the neutral sheet. These central modes develop into a fairly strong structure compared to the side modes.

The temporal evolution of the Fourier mode of electric field E_x is shown in Fig. 6. The implication of this figure is the following. First, the electric perturbations stay almost at the same places on the y axis and do not propagate in the y direction and are more dominant on the higher modes ($m_x = 5$ or 6). Secondly, comparing Fig. 5 and Fig. 6, one can find that the side modes (the LHDI modes) present a more electrostatic nature, while the central modes are dominant for lower modes ($m_x = 1$ and 2) and exhibit a more magnetic nature.

C. New low frequency electromagnetic instability

In order to study whether the low frequency mode at the field null region is the nonlinear mode caused by the LHDI or a new instability mode, we have performed a simulation run in which the fast growing LHD modes (m$\geq$4) are artificially eliminated. Figure 7 shows the time sequential plots of the magnetic field contours and the perturbed magnetic field contours. The meandering structure corresponding to the low frequency electromagnetic mode at the field null region is generated after $t = 2800\ \omega_{pe0}^{-1}$. Also shown in Fig. 8 is the temporal evolution of Fourier modes of the magnetic and electric fields, B_z, E_x. The mode of the field null region grows and exhibits a similar pattern to that of Figs. 5 and 6. From these results we come to the conclusion that the growth of LHDI does not affect the growth of the low frequency electromagnetic mode at the field null region. Thus, it is concluded that the low frequency, central mode is a new mode.

In order to examine the dependence of the system size on the newly found mode, we have performed a run whose simulation size in $x-$direction L_x is twice as large as that in the typical runs, i.e., $L_x = 60\ c/\omega_{pe0}$ and the grid number in the $x-$direction is 131. Figure 9 shows the time sequential plots of the magnetic field and the perturbed magnetic field. The meandering structure is observed after $T = 2800\ \omega_{pe0}^{-1}$. Figure 10 shows the temporal evolution of the Fourier amplitude of the magnetic field B_z. The dominant mode is obviously $\mathrm{m}_x = 4$. Remembering that the dominant mode in the run with $L_x = 30\ c/\omega_{pe0}$ is $\mathrm{m}_x = 2$, we can conclude that the wavelength of the dominant mode does not depend on the simulation length, namely, that the observed meandering structure of the field

null region is an intrinsic process of the neutral sheet.

Let us consider the characteristic time governing the development of the meandering structure of the magnetic field in the neutral sheet region. The time of the present simulation is normalized by the electron plasma frequency ω_{pe}. However, since the observed slow phenomenon seems to be independent of the electron time scale, we shall replot the characteristic time (T_m) of the meandering structure in terms of the ion gyro period, $T_{ci} = 2\pi\Omega_{ci}^{-1}$. Examining the data of the results of Tananka and Sato[11], and Winske[9], Brackbill *et al.*[12], we obtain $T_m \sim 0.39\ T_{ci}$ ($(\omega_{pe}/\Omega_{ce})^2 = 0.55,\ m_i/m_e = 185$), $0.44\ T_{ci}$ ($\Omega_{ce}/\omega_{pe} \sim 0.5,\ m_i/m_e = 100$). and $\sim 0.32T_{ci}$ ($\omega_{pe}/\Omega_{ce} = 9.9,\ m_i/m_e = 100$), respectively. We may thus infer that the time required for the meandering structure to become sizable is on the order of T_{ci}. In our case the characteristic time is $T_m \approx 2000\ \omega_{pe0}^{-1} \approx 0.54T_{ci}$. Besides, the frequency of the present electromagnetic wave in the neutral sheet is about $0.47\Omega_{ci0}$. These results suggest that the new low frequency electromagnetic instability in the neutral sheet is strongly related to the ion cyclotron motion.

Winske[9] pointed out three probable origins of the instability at the field null region. One is that the turbulence on both sides of the field null region heats the particles near the null point anisotropically to drive a Weibel instability[17]. However, this possibility should be rejected, because the electron distribution function in the field reversal region exhibits no appreciable anisotropy. A second possibility is that the nonlinear penetration of the LHDI causes this electromagnetic instability. As seen in the previous subsection, this possibility cannot be accepted either. A third possibility, which was proposed by Yamanaka[18], is that ions with

the meandering orbits would play an important role in triggering an instability. Considering the fact that the required time for occurrence of the electromagnetic instability in the neutral sheet, this third possibility appears to be the most probable. The meandering motion of ions can resonate with electromagnetic fluctuations to excite them. Substituting the parameters of the present simulation into Yamanaka's formula, the frequency of the dominent mode $m_x = 2$ is given by roughly $9.3 \times 10^{-3}\ \Omega_{ce0}$, which is about three times as large as the frequency obtained from the simulation, $2.62 \times 10^{-3}\ \Omega_{ce0}$. Since Yamanaka approximated the magnetic field near the neutral sheet as a linear function to carry out the orbit-integral analytically and took the limit that the ion drift velocity is much larger than the ion thermal velocity. In other words, the effct of complicated meandering motion was very poorly evaluated, which may make a considerable error. Nevertheless, judging from the overall circumstantial conditions, it appears that the electromagnetic instability can be caused by the ion meandering motion[19].

D. Anomalous resistivity

Since the appearance of the $m_x = 0$ mode of the electric field is indicative of generation of anomalous resistivity, we shall here examine the temporal behavior of this zero mode with particular attention. Figure 11 represents its behavior. In the early period, the growth of the $m_x = 0$ electric field mode caused by the LHDI is observed on both sides of the neutral sheet region, but no electric field at the field null region is observed. With the passage of time, the $m_x = 0$ electric field decays but the new $m_x = 0$ mode appears at the field null region. This $m_x = 0$ mode of electric field at the field null region is associated with the

new electromagnetic mode at the field null region. This appearance of the new electromagnetic mode must be related to the generation of anomalous resistivity at the field null region.

We shall here evaluate the amount of the anomalous resistivity caused by the new electromagnetic instability. Figure 12 shows the temporal evolution of $\mathrm{m}_x = 0$ Fourier mode of the electric field E_x, the electric current J_x, and the resistivity at $y = 0$. The enhancement of the E_x ($\mathrm{m}_x = 0$) is observed around $t = 4000\ \omega_{pe0}^{-1}$ when the new electromagnetic mode is dominantly excited. The electric current increases to the peak at $T \sim 3000\ \omega_{pe0}^{-1}$ and gradually decays afterwards. By comparing the temporal behaviors of E_x ($\mathrm{m}_x = 0$) and J_x ($\mathrm{m}_x = 0$), one can obtain the value of the anomalous resistivity η to be of the order of $0.002\omega_{pe0}^{-1}$ during the time from $T \approx 4000\ \omega_{pe0}$ to $T \approx 12000\ \omega_{pe0}$.

4. CONCLUSION

We have investigated electromagnetic waves in a magnetic neutral sheet by means of a $2\frac{1}{2}$ semi-implicit particle simulation code. The main results are summarized as follows.

(1) A low frequency electromagnetic wave is excited in a magnetically null sheet region after the decay of the lower hybrid (electrostatic) drift instability excited in the region away from the neutral sheet. Generation of this electromagnetic instability is not related to the LHDI. (2) The generated anomalous resistivity in the neutral sheet is estimated to be $\eta \approx 2 \times 10^{-3}\ \omega_{pe}^{-1}$. (3) The instability develops into a meandering structure of the neutral sheet. (4) The meandering structure develops into a sizable structure roughly in one cyclotron

period. (5) The frequency of this mode is of the order of the ion cyclotron frequency. (6) This mode may be caused by the meandering motion of ions.

The present simulation study thus concludes that a low frequency electromagnetic instability is excited at the field null region and generates anomalous resistivity in the magnetic neutral sheet, which might cause collisionless reconnection.

ACKNOWLEDGMENTS

This work was supported by the Ministry of Education, Science and Culture Grants-in-Aid No. 07832024. One of the authors (M.O) would like to thank Dr. S. Murakami for guidance of the simulation code.

REFERENCES

[1] T. Sato and H. Hayashi: Phys. Fluids **22**(1979)1189.

[2] R. Horiuchi and T. Sato: Phys. Plasmas 1(1994)3587.

[3] N. A. Krall and D. L. Book: Phys. Rev. Lett. **23**(1969)574.

[4] T. Sato and H. Okuda: Phys. Rev. Lett. **44** (1980)740.

[5] N. A. Krall and P. C. Liewer: Phys. Rev. 4 2094 (1971)2094.

[6] R. C. Davidson and N. T. Gladd: Phys. Fluids **18** (1975)1327.

[7] J. D. Huba, N. T. Gladd, and K. Papadopoulous: J. Geophys. Res. **83** (1978)5217.

[8] R. C. Davidson, N. T. Gladd, C. S. Wu, and J. D. Huba: Phys. Fluids **20**(1977)301.

[9] D. Winske, Phys. Fluids: **24**(1981)1069.

[10] M. Tanaka and T. Sato: Phys. Rev. Lett. **47**(1981)714.

[11] M. Tanaka and T. Sato: J. Geophys. Res. **86**(1981)5541.

[12] J. U. Brackbill, D. W. Forslund, K. B. Quest, and D. Winske: Phys. Fluids **27**(1984)2682.

[13] J. D. Huba, J. F. Drake, and N. T. Gladd: Phys. Fluids**23** (1980)552.

[14] M. Tanaka: J. Compt. Phys. **79**(1988)209.

[15] S. Murakami and T. Sato: J. Phys. Soc. Jpn. **61**(1992)849.

[16] E. Harris: Nuovo Cimento **23**(1962)115.

[17] E. S. Weibelr: Phys. Rev. Lett. **2**(1959)83.

[18] K. Yamanaka: Phys. Scripta **17**(1978)15.

[19] R. Horiuchi and T. Sato: Phys. Fluids **B2**(1990)2652.

FIGURE CAPTIONS

Fig. 1: Time sequential plots of (left) the magnetic field contours and (right) the perturbed magnetic field contours.

Fig. 2: Time sequential plots of (left) E_x contours and (right) E_y contours.

Fig. 3: Time sequential plots of the electron flow velocities.

Fig. 4: (a) Dispersion relation of E_x at $y = 5\ c/\omega_{pe0}$ (circle). The solid curve is the theoretical dispersion relation for the LHDI. The frequency is normalized by the lower hybrid frequency at $y = 5\ c/\omega_{pe0}$. (b) Dispersion relation of B_x at $y = 0\ c/\omega_{pe0}$ (square). The frequncy is normalized by the ion cyclotron frequency Ω_{ci0}.

Fig. 5: The color-coded contour map of the Fourier components of the magnetic field in the time (T)-space(y) domain.

Fig. 6: The color-coded map of the Fourier components of the electric field in the time(T)-space(y) domain.

Fig. 7: Time sequential plots of (left) the magnetic field contours and (right) the perturbed magnetic field contours when the $m_x \geq 4$ modes are eliminated.

Fig. 8: The color-coded contour map of the Fourier components of the magnetic field and the electric field in the time(T)-space(y) domain when the $m_x \geq 4$ modes are eliminated.

Fig. 9: Time sequential plots of (left) the magnetic field contours and (right) the perturbed magnetic field contours for the $L_x = 60\ c/\omega_{pe0}$.

Fig. 10: Temporal evolutions of the Fourier amplitudes of B_x for (a) $L_x = 30\ c/\omega_{pe0}$ and (b) $L_x = 60\ c/\omega_{pe0}$.

Fig. 11: The color-coded contour map of the $m_x = 0$ mode of the electric field in the time(T)-space(y) domain: (a)$-15 \leq y \leq 15$ (b) $-5 \leq y \leq 5$.

Fig. 12: Temporal evolutions of the $m_x = 0$ Fourier modes of E_x, J_x, and η at $y = 0$.

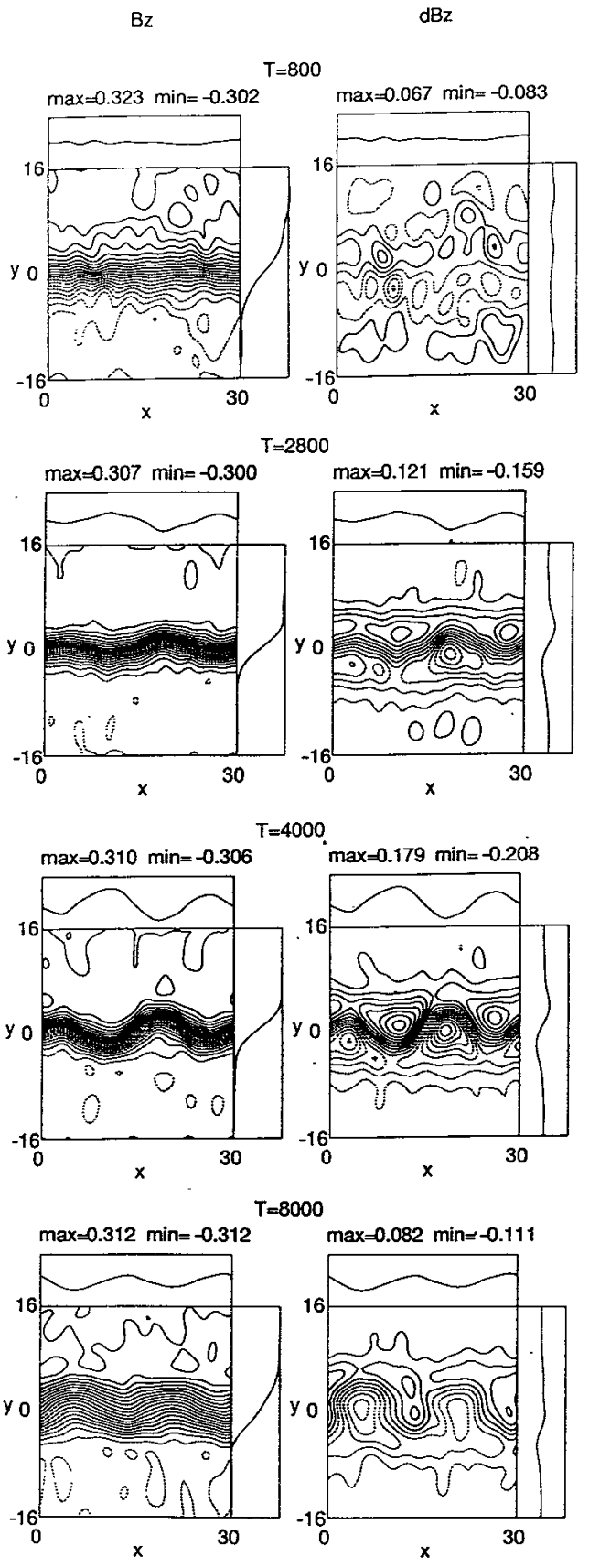
Bz
dBz
T=800
max=0.323 min= -0.302
max=0.067 min= -0.083
T=2800
max=0.307 min= -0.300
max=0.121 min= -0.159
T=4000
max=0.310 min= -0.306
max=0.179 min= -0.208
T=8000
max=0.312 min= -0.312
max=0.082 min= -0.111
16
y 0
-16
0
30
x

Fig. 1

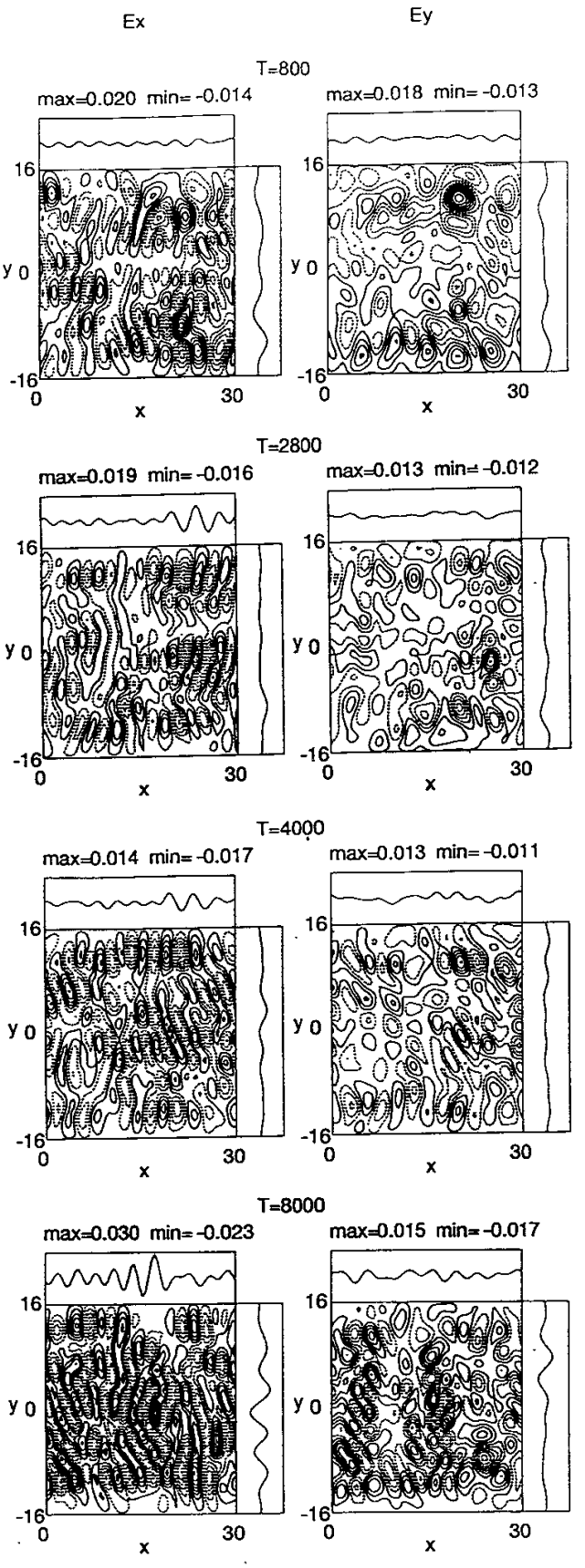
Ex
Ey
T=800
max=0.020 min= -0.014
max=0.018 min= -0.013
T=2800
max=0.019 min= -0.016
max=0.013 min= -0.012
T=4000
max=0.014 min= -0.017
max=0.013 min= -0.011
T=8000
max=0.030 min= -0.023
max=0.015 min= -0.017
16
y 0
-16
0
30
x

Fig. 2

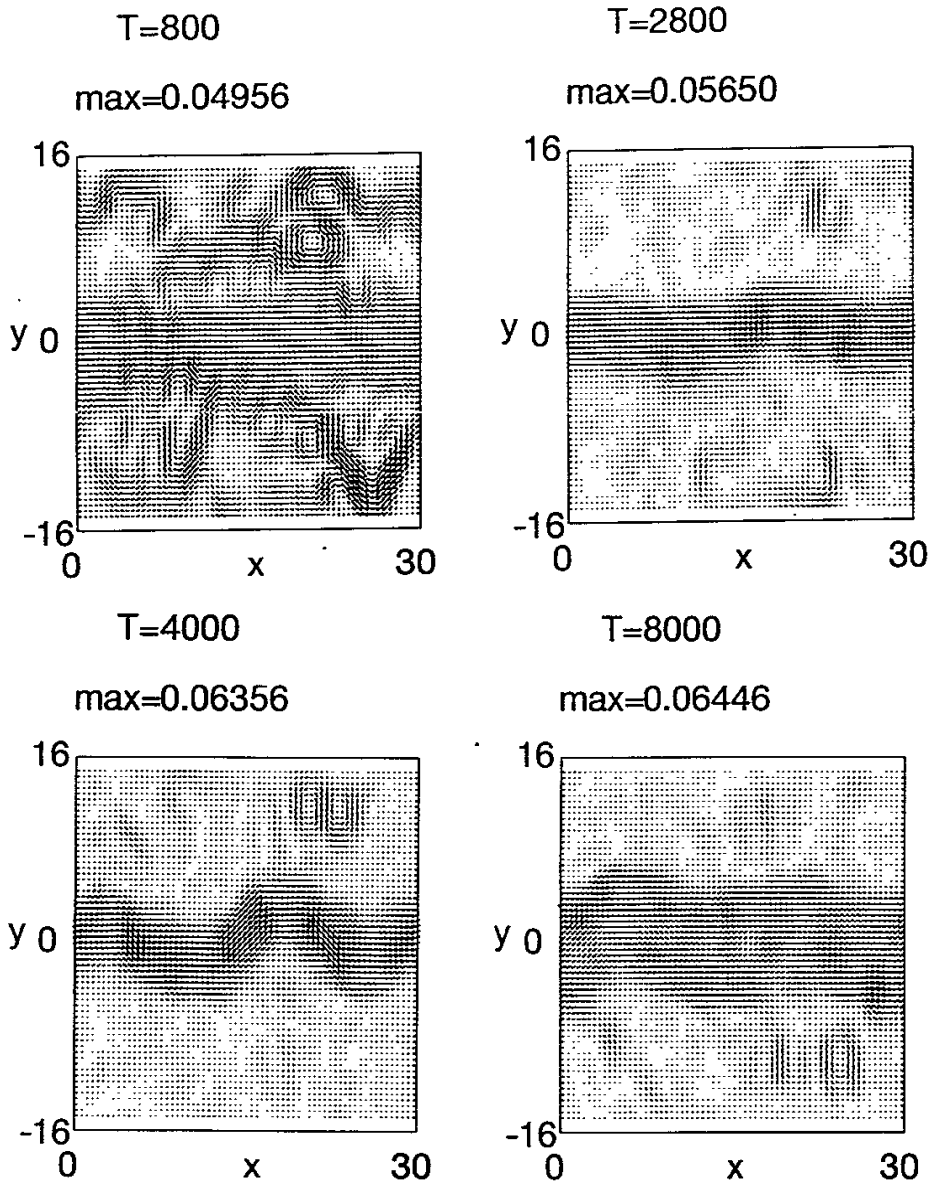
T=800
max=0.04956
16
y 0
-16
0
x
30
T=2800
max=0.05650
16
y 0
-16
0
x
30
T=4000
max=0.06356
16
y 0
-16
0
x
30
T=8000
max=0.06446
16
y 0
-16
0
x
30

Fig. 3

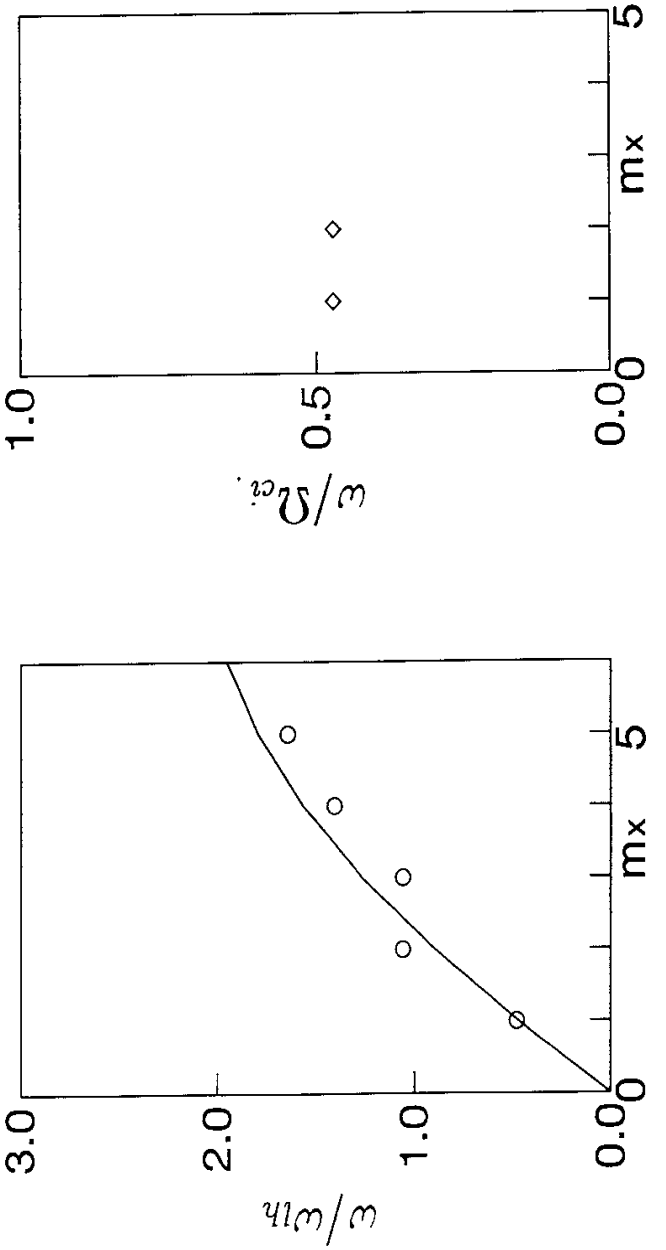

Fig. 4

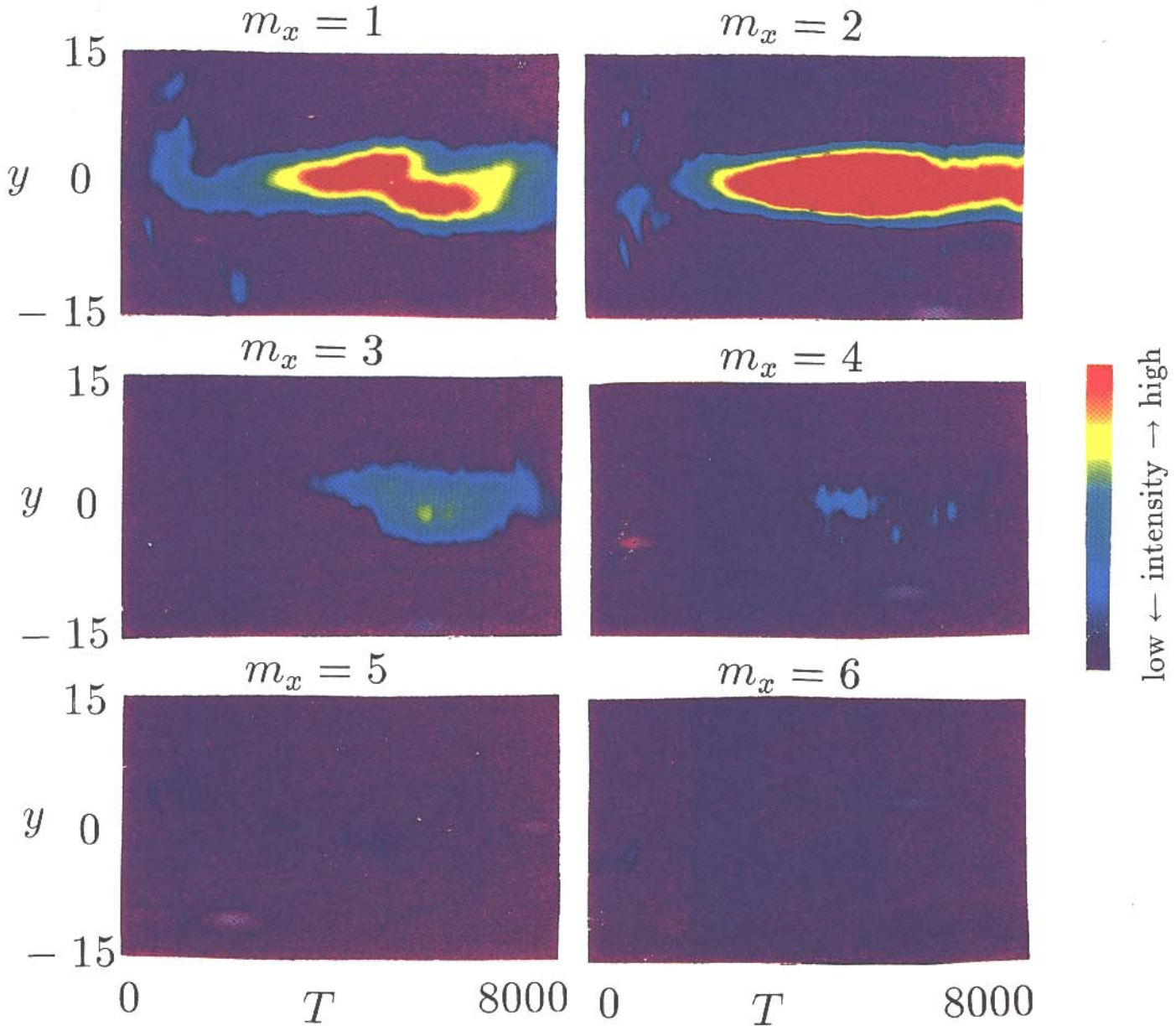

Fig. 5

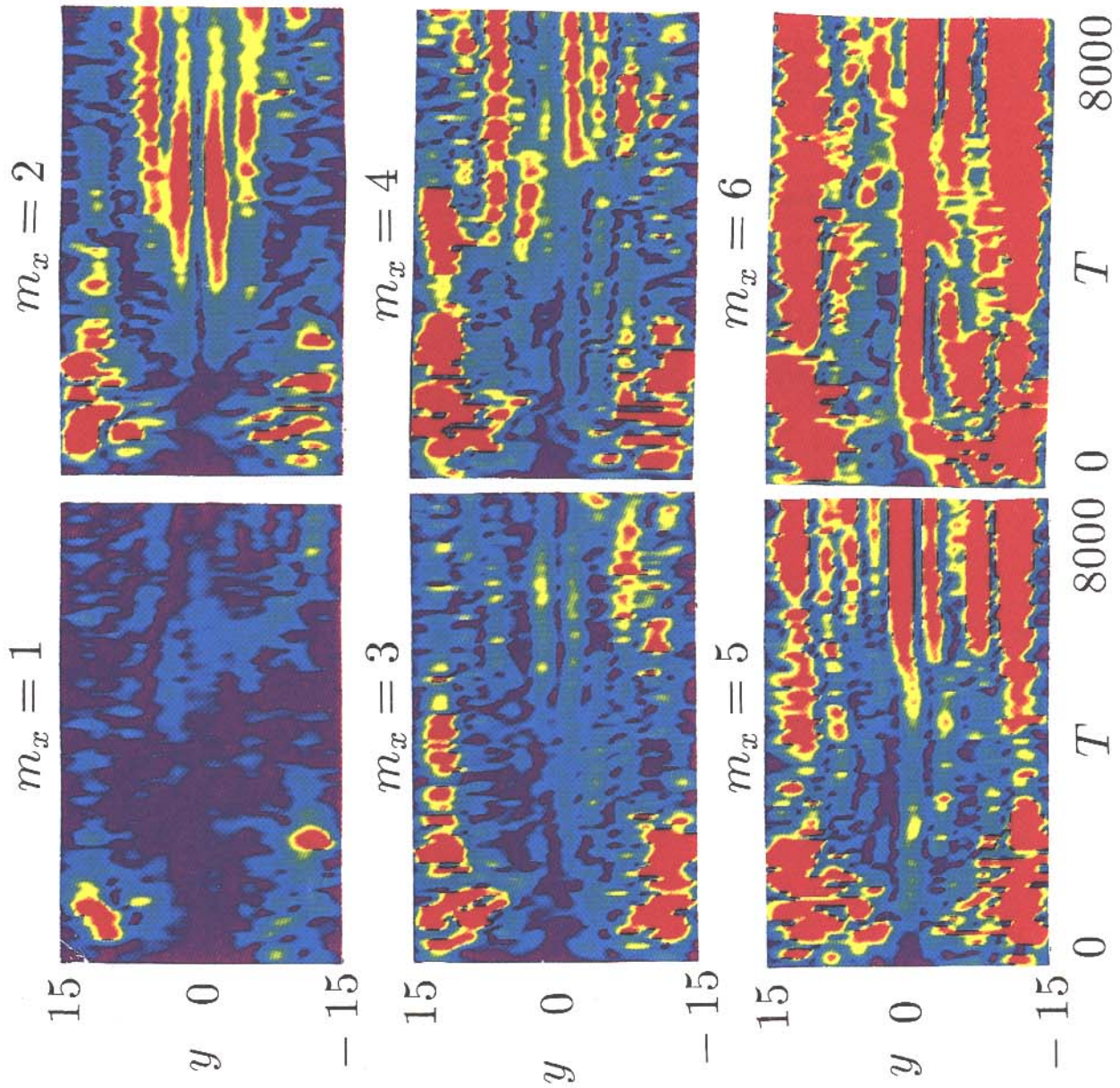

Fig. 6

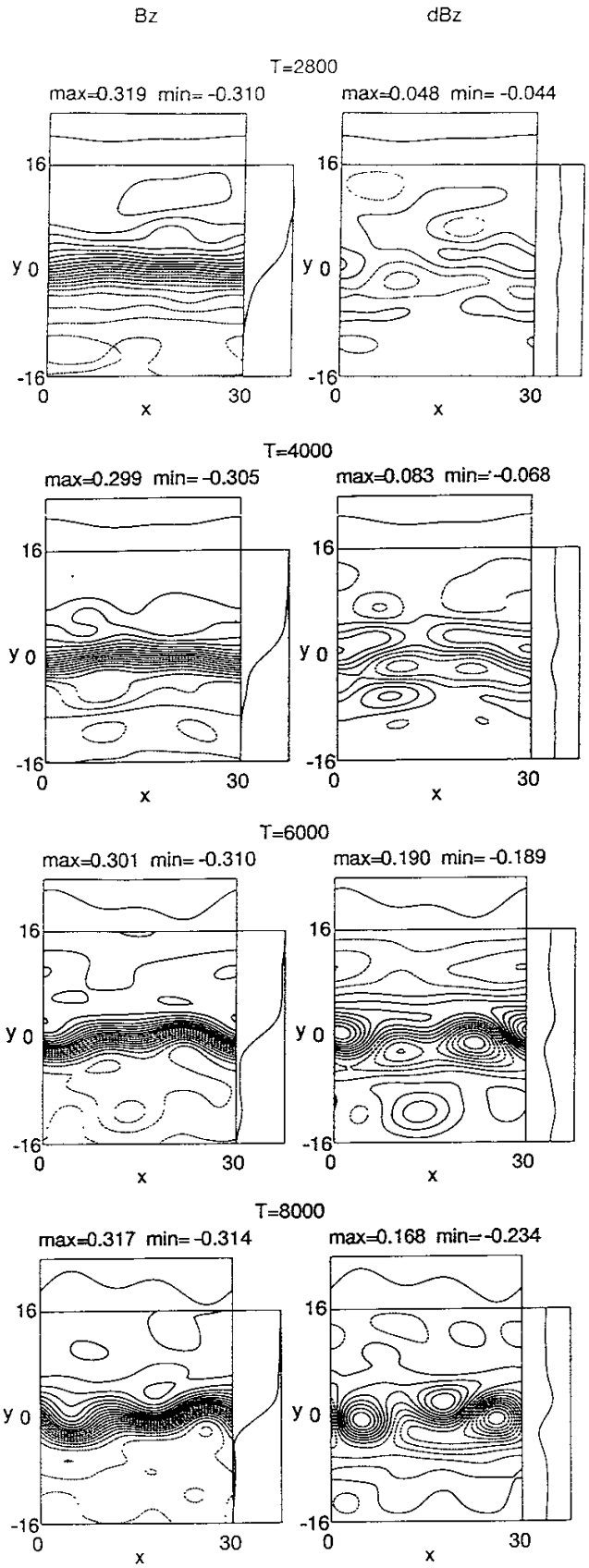
Bz
dBz
T=2800
max=0.319 min= -0.310
max=0.048 min= -0.044
T=4000
max=0.299 min= -0.305
max=0.083 min= -0.068
T=6000
max=0.301 min= -0.310
max=0.190 min= -0.189
T=8000
max=0.317 min= -0.314
max=0.168 min= -0.234
16
y 0
-16
0
30
x

Fig. 7

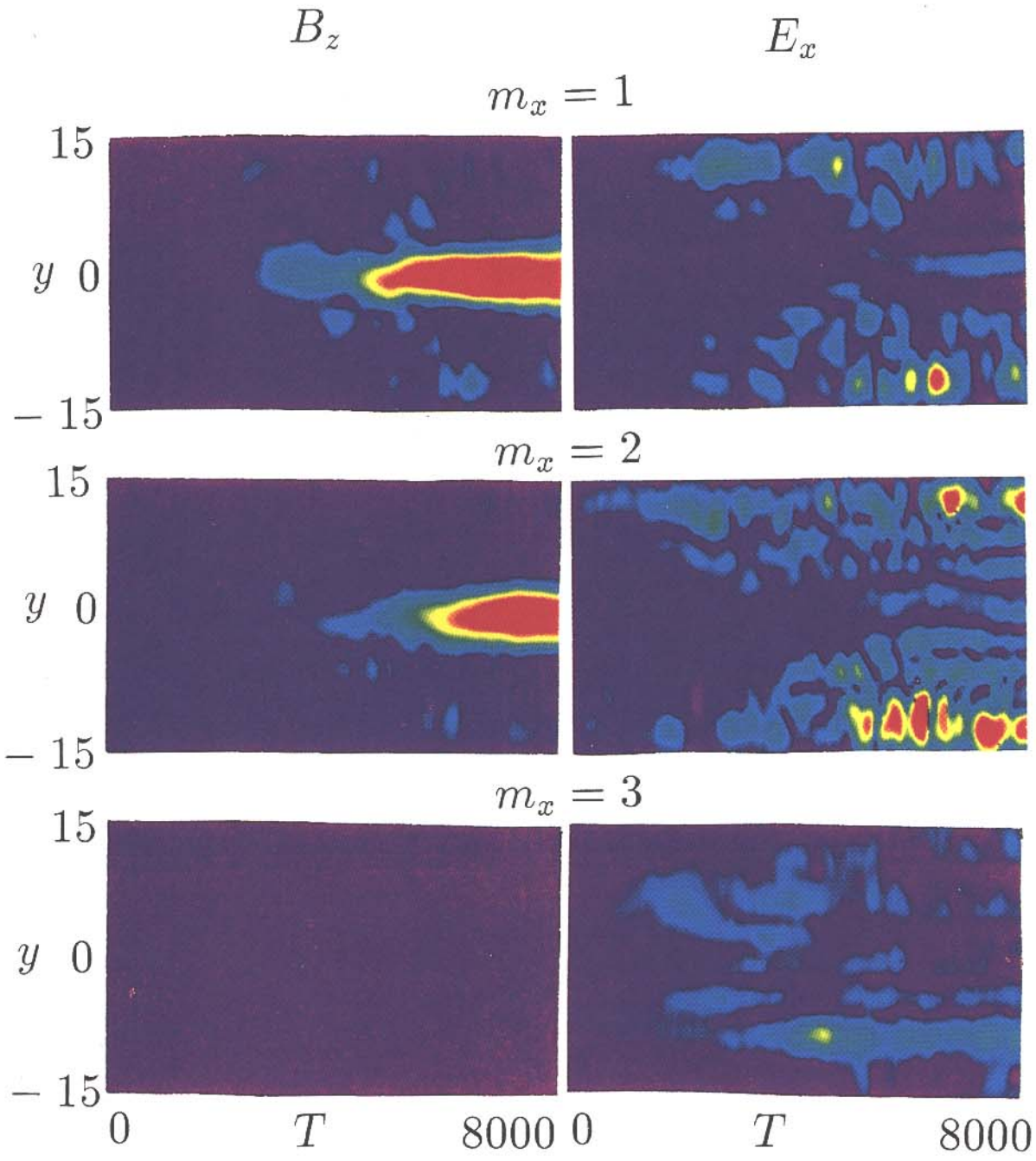

Fig. 8

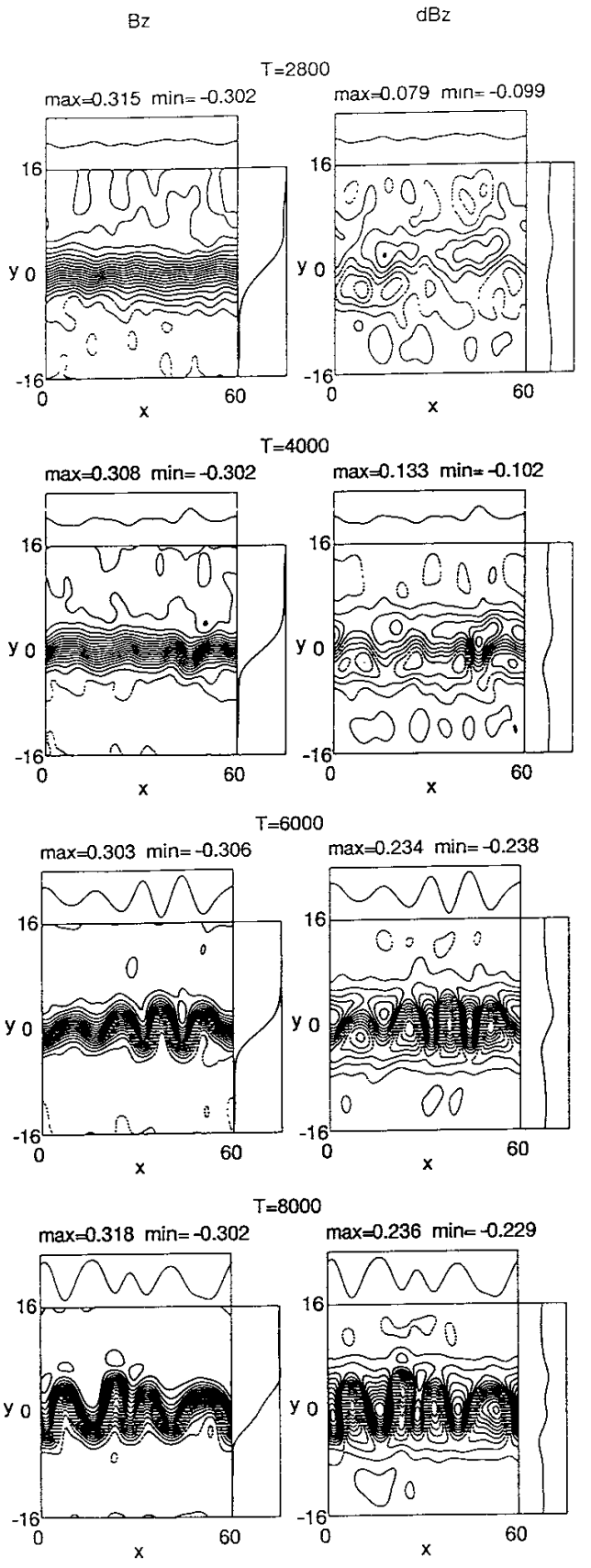
Bz
dBz
T=2800
max=0.315 min= -0.302
max=0.079 min= -0.099
T=4000
max=0.308 min= -0.302
max=0.133 min= -0.102
T=6000
max=0.303 min= -0.306
max=0.234 min= -0.238
T=8000
max=0.318 min= -0.302
max=0.236 min= -0.229
16
y 0
-16
0
60
x

Fig. 9

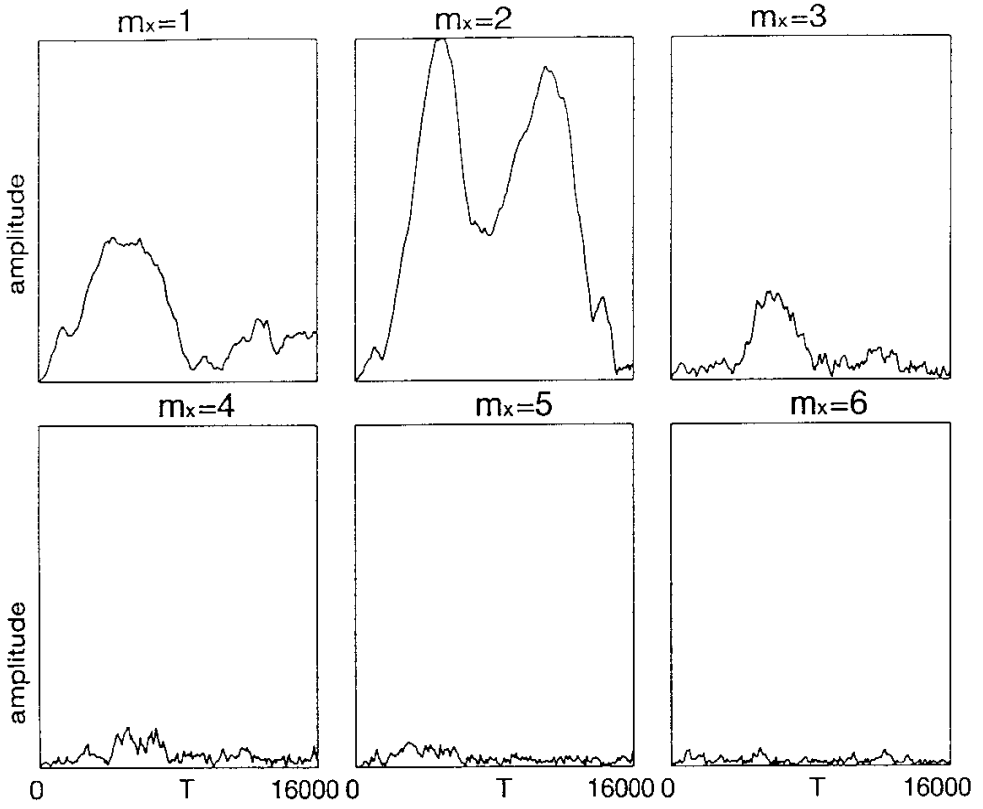

(a) $L_x = 30$

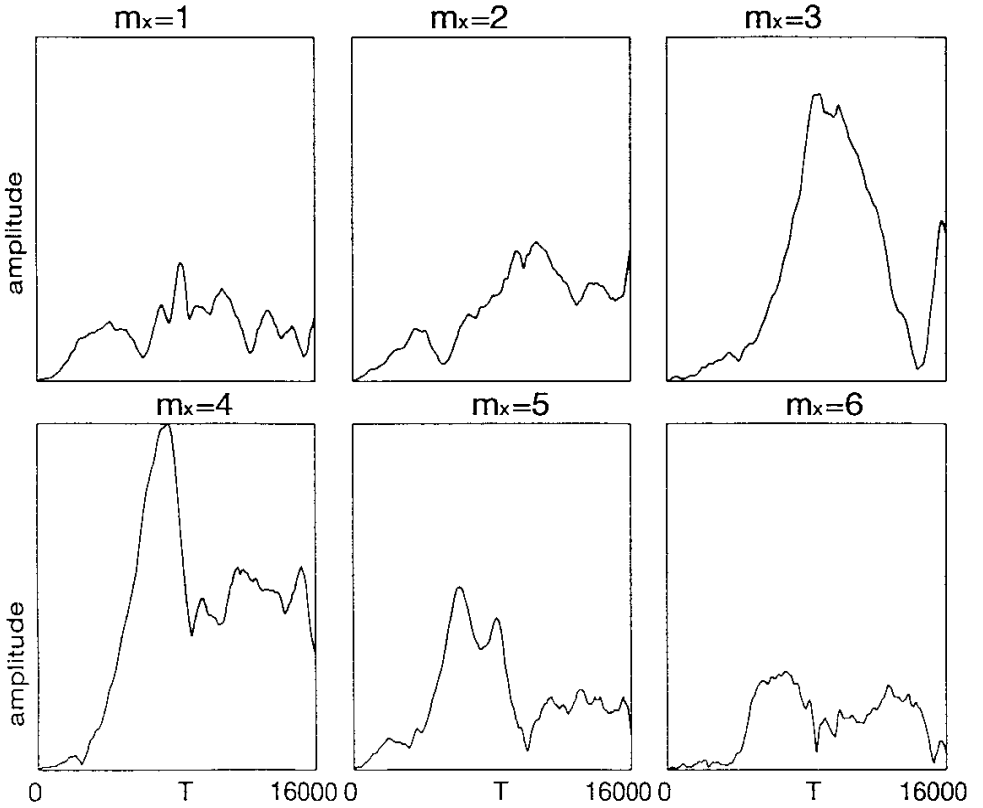

(b) $L_x = 60$

Fig. 10

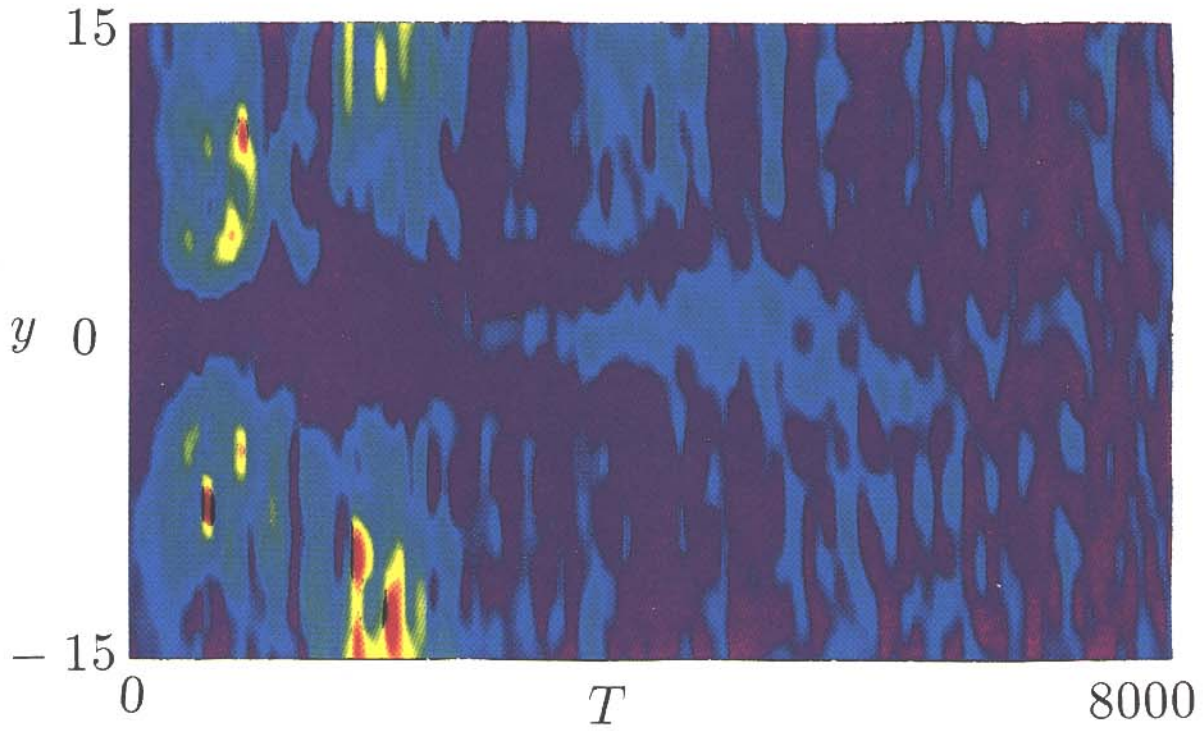

(a)

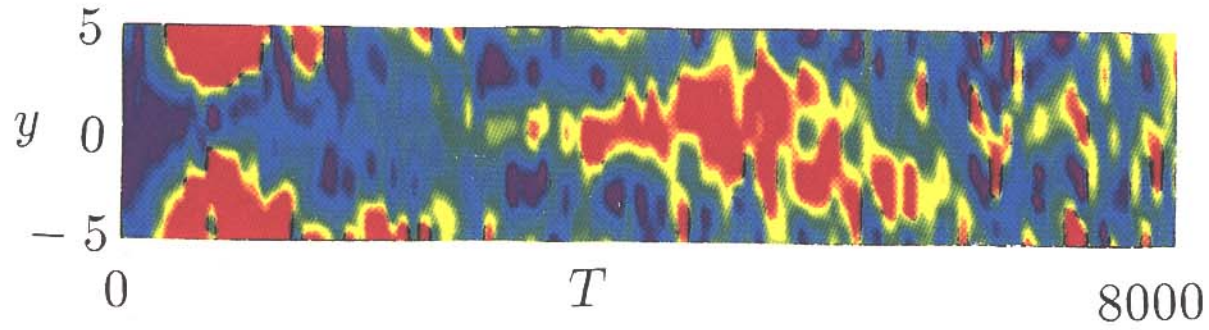

(b)

Fig. 11

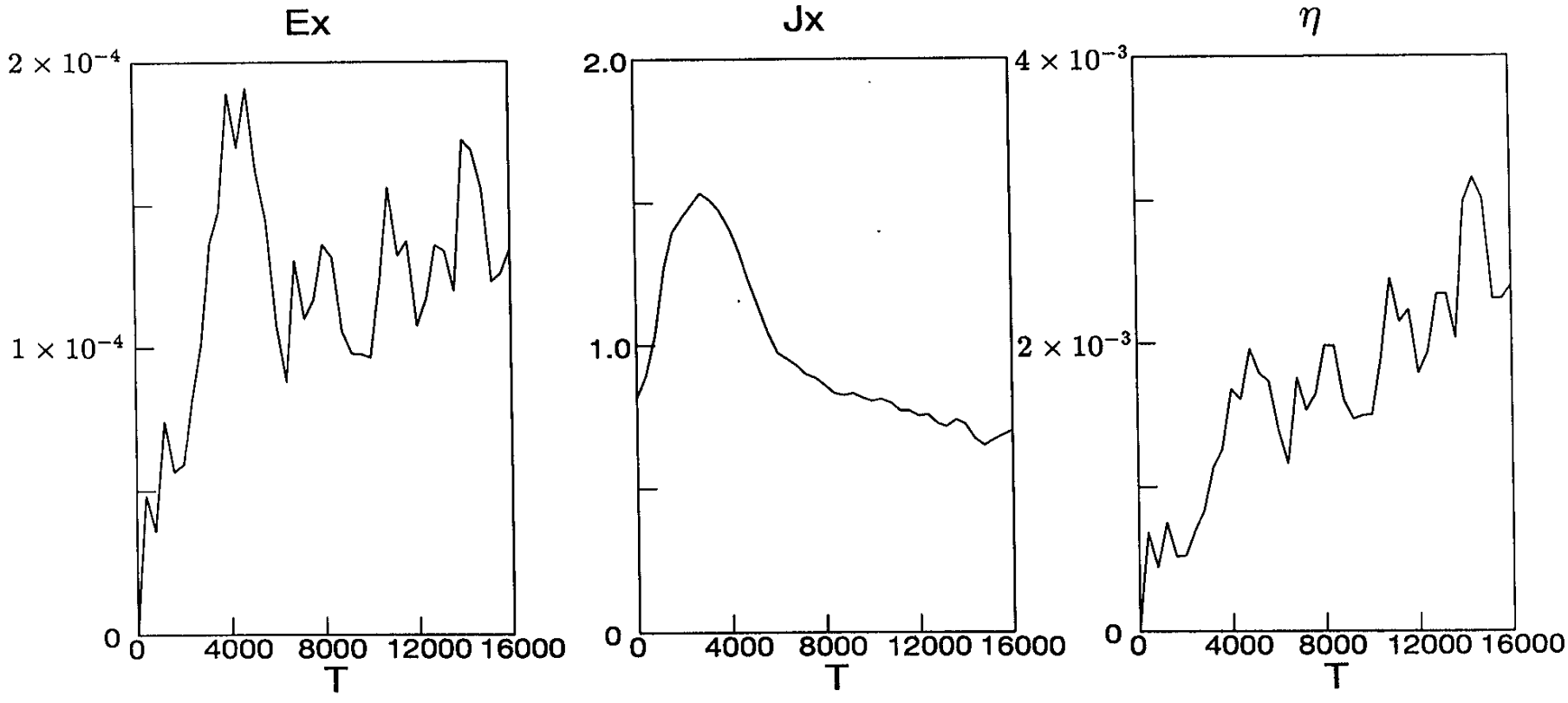
Ex
2×10^{-4}
1×10^{-4}
0
0
4000
8000
12000
16000
T
Jx
2.0
1.0
0
0
4000
8000
12000
16000
T
η
4×10^{-3}
2×10^{-3}
0
0
4000
8000
12000
16000
T

Fig. 12

NIFS-358 M. Ida and T. Yabe,
Implicit CIP (Cubic-Interpolated Propagation) Method in One Dimension; May 1995

NIFS-359 A. Kageyama, T. Sato and The Complexity Simulation Group,
Computer Has Solved A Historical Puzzle: Generation of Earth's Dipole Field; June 1995

NIFS-360 K. Itoh, S.-I. Itoh, M. Yagi and A. Fukuyama,
Dynamic Structure in Self-Sustained Turbulence; June 1995

NIFS-361 K. Kamada, H. Kinoshita and H. Takahashi,
Anomalous Heat Evolution of Deuteron Implanted Al on Electron Bombardment; June 1995

NIFS-362 V.D. Pustovitov,
Suppression of Pfirsch-schlüter Current by Vertical Magnetic Field in Stellarators. June 1995

NIFS-363 A. Ida, H. Sanuki and J. Todoroki
An Extended K-dV Equation for Nonlinear Magnetosonic Wave in a Multi-Ion Plasma; June 1995

NIFS-364 H. Sugama and W. Horton
Entropy Production and Onsager Symmetry in Neoclassical Transport Processes of Toroidal Plasmas; July 1995

NIFS-365 K. Itoh, S.-I. Itoh, A. Fukuyama and M. Yagi,
On the Minimum Circulating Power of Steady State Tokamaks; July 1995

NIFS-366 K. Itoh and Sanae-I. Itoh,
The Role of Electric Field in Confinement; July 1995

NIFS-367 F. Xiao and T. Yabe,
A Rational Function Based Scheme for Solving Advection Equation; July 1995

NIFS-368 Y. Takeiri, O. Kaneko, Y. Oka, K. Tsumori, E. Asano, R. Akiyama, T. Kawamoto and T. Kuroda,
Multi-Beamlet Focusing of Intense Negative Ion Beams by Aperture Displacement Technique; Aug. 1995

NIFS-369 A. Ando, Y. Takeiri, O. Kaneko, Y. Oka, K. Tsumori, E. Asano, T. Kawamoto, R. Akiyama and T. Kuroda,
Experiments of an Intense H- Ion Beam Acceleration; Aug. 1995

NIFS-370 M. Sasao, A. Taniike, I. Nomura, M. Wada, H. Yamaoka and M. Sato,

Development of Diagnostic Beams for Alpha Particle Measurement on ITER; Aug. 1995

NIFS-371 S. Yamaguchi, J. Yamamoto and O. Motojima;
A New Cable -in conduit Conductor Magnet with Insulated Strands; Sep. 1995

NIFS-372 H. Miura,
Enstrophy Generation in a Shock-Dominated Turbulence; Sep. 1995

NIFS-373 M. Natsir, A. Sagara, K. Tsuzuki, B. Tsuchiya, Y. Hasegawa, O. Motojima,
Control of Discharge Conditions to Reduce Hydrogen Content in Low Z Films Produced with DC Glow; Sep. 1995

NIFS-374 K. Tsuzuki, M. Natsir, N. Inoue, A. Sagara, N. Noda, O. Motojima, T. Mochizuki, I. Fujita, T. Hino and T. Yamashina,
Behavior of Hydrogen Atoms in Boron Films during H_2 and He Glow Discharge and Thermal Desorption; Sep. 1995

NIFS-375 U. Stroth, M. Murakami, R.A. Dory, H. Yamada, S. Okamura, F. Sano and T. Obiki,
Energy Confinement Scaling from the International Stellarator Database; Sep. 1995

NIFS-376 S. Bazdenkov, T. Sato, K. Watanabe and The Complexity Simulation Group,
Multi-Scale Semi-Ideal Magnetohydrodynamics of a Tokamak Plasma; Sep. 1995

NIFS-377 J. Uramoto,
Extraction of Negative Pionlike Particles from a H2 or D2 Gas Discharge Plasma in Magnetic Field; Sep. 1995

NIFS-378 K. Akaishi,
Theoretical Consideration for the Outgassing Characteristics of an Unbaked Vacuum System; Oct. 1995

NIFS-379 H. Shimazu, S. Machida and M. Tanaka,
Macro-Particle Simulation of Collisionless Parallel Shocks; Oct. 1995

NIFS-380 N. Kondo and Y. Kondoh,
Eigenfunction Spectrum Analysis for Self-organization in Dissipative Solitons; Oct. 1995

NIFS-381 Y. Kondoh, M. Yoshizawa, A. Nakano and T. Yabe,
Self-organization of Two-dimensional Incompressible Viscous Flow in a Friction-free Box; Oct. 1995

NIFS-382 Y.N. Nejoh and H. Sanuki,
The Effects of the Beam and Ion Temperatures on Ion-Acoustic Waves in

an Electron Beam-Plasma System; Oct. 1995

NIFS-383 K. Ichiguchi, O. Motojima, K. Yamazaki, N. Nakajima and M. Okamoto
Flexibility of LHD Configuration with Multi-Layer Helical Coils;
Nov. 1995

NIFS-384 D. Biskamp, E. Schwarz and J.F. Drake,
Two-dimensional Electron Magnetohydrodynamic Turbulence; Nov. 1995

NIFS-385 H. Kitabata, T. Hayashi, T. Sato and Complexity Simulation Group,
Impulsive Nature in Collisional Driven Reconnection; Nov. 1995

NIFS-386 Y. Katoh, T. Muroga, A. Kohyama, R.E. Stoller, C. Namba and O. Motojima,
Rate Theory Modeling of Defect Evolution under Cascade Damage Conditions:The Influence of Vacancy-type Cascade Remnants and Application to the Defect Production Chracterization by Microstructural Analysis; Nov. 1995

NIFS-387 K. Araki, S. Yanase and J. Mizushima,
Symmetry Breaking by Differential Rotation and Saddle-node Bifurcation of the Thermal Convection in a Spherical Shell; Dec. 1995

NIFS-388 V.D. Pustovitov,
Control of Pfirsch-Schlüter Current by External Poloidal Magnetic Field in Conventional Stellarators: Dec. 1995

NIFS-389 K. Akaishi,
On the Outgassing Rate Versus Time Characteristics in the Pump-down of an Unbaked Vacuum System; Dec. 1995

NIFS-390 K.N. Sato, S. Murakami, N. Nakajima, K. Itoh,
Possibility of Simulation Experiments for Fast Particle Physics in Large Helical Device (LHD); Dec. 1995

NIFS-391 W.X.Wang, M. Okamoto, N. Nakajima, S. Murakami and N. Ohyabu,
A Monte Carlo Simulation Model for the Steady-State Plasma in the Scrape-off Layer; Dec. 1995

NIFS-392 Shao-ping Zhu, R. Horiuchi, T. Sato and The Complexity Simulation Group,
Self-organization Process of a Magnetohydrodynamic Plasma in the Presence of Thermal Conduction; Dec. 1995

NIFS-393 M. Ozaki, T. Sato, R. Horiuchi and the Complexity Simulation Group
Electromagnetic Instability and Anomalous Resistivity in a Magnetic Neutral Sheet; Dec. 1995